Journal of The Electrochemical Society, **152** (11) A2114-A2122 (2005)
0013-4651/2005/152(11)/A2114/9/$7.00 © The Electrochemical Society, Inc.

Distributed Performance of Polymer Electrolyte Fuel Cells under Low-Humidity Conditions

Q. Dong,[a,*] M. M. Mench,[a,,z] S. Cleghorn,[b] and U. Beuscher[b]**

[a]*Fuel Cell Dynamics and Diagnostics Laboratory, Department of Mechanical and Nuclear Engineering, The Pennsylvania State University, University Park, Pennsylvania 16802, USA*
[b]*W.L. Gore & Associates, Gore Fuel Cell Technologies, Incorporated, Elkton, Maryland 21921, USA*

For reduced system complexity and compactness, it is desirable to operate polymer electrolyte fuel cells (PEFC) with low humidification. In order to more fully understand and optimize performance, there is a need for combined distributed current, species, and impedance data. This paper presents results of a series of experiments at various anode and cathode humidity levels with distributed current, species, and high frequency resistance (HFR) data. This provides much insight into the characteristic operating performance of PEFCs under low-humidity operation. Results show that the degree of water saturation in the anode greatly influences local performance through local anode dryout, even for the thin 18 μm electrolytes used in this study. A characteristic curve has been developed to predict the qualitative shape of the current profile for a coflow arrangement under fully dry to fully humidified inlet combinations. These results should also be of great interest to those seeking experimental data for model validation.
 [DOI: 10.1149/1.2039628]

Manuscript submitted December 29, 2004; revised manuscript received June 6, 2005. Available electronically September 8, 2005.

The hydrogen polymer electrolyte fuel cell (PEFC) has tremendous promise as a future power system due to its low pollution, high efficiency, and stealth. Many studies, too numerous to list completely, have examined various aspects of PEFC performance as a function of operating conditions.[1-14] The reader is referred to Ref. 15 and 16 for more comprehensive reviews on PEFC fundamentals. In addition to experimental characterization, much research has been focused on *first-principles-based* modeling of the PEFC system.[17-33] However, advances in modeling of the PEFC have thus far outpaced the ability to experimentally verify the predicted performance. In particular, scant experimental data are presently available regarding current density, species, and ohmic resistance distributions. If taken together, this combination of distributed data can reveal a great deal of information about the localized water transport, performance, failure modes, and cell design. This type of detailed data must be obtained to provide complex model validation and permit an ultimate understanding of the physicochemical phenomena in PEFCs.

Several previous publications have examined the distributed current in a PEFC using various methods including segmented current collectors,[34-38] magnetic loop arrays,[39,40] masking, isolating, or segmented electrodes,[41] or printed circuit board techniques.[42] While current density distribution alone is highly revealing, knowledge of the mass distribution is also critical to understanding water management and reactant distribution effects. Many authors have conducted detailed studies or deduced models that describe the water transport through fuel cell components, including the electrolyte and porous gas diffusion layers (GDLs),[43-59] but scant experimental detail is available in operating fuel cells.

A few authors have completed detailed studies of the water balance in an operating cell by collection of the fuel cell effluent, and condensation of the gas-phase water vapor.[60-63] While insightful, these studies do not provide data on the water distribution throughout the working cell, which could vary widely depending on operating conditions, current and temperature distribution, and local nonisotropic transport parameters. Recently, Mench and co-workers have demonstrated two new techniques for in situ measurement of distributed species data, including saturated water content up to 90°C.[64,65] In the gas chromatograph (GC) method, only steady-state data can be obtained, while in the real-time gas analysis (RTGA) method, real-time (1 Hz) data can be obtained to reveal the water and other species transport dynamics in the flow channel.

In addition to current and species distributions, an understanding of the local hydration state of the electrolyte is important to delineate membrane resistance losses from gas-phase mass transport and liquid water flooding effects. Commonly in fuel cell research, the tool of high-frequency resistance (HFR) has been used to determine the bulk resistance of a PEFC, and thus glean information about the overall state of hydration of the electrolyte. While this technique is useful to delineate reactant transport and cell compression from electrolyte hydration and degradation losses, the same data on a localized distributed scale can provide much more information about the locations of membrane hydration, flooding, and degradation.

In some applications, it may be desirable to operate under low-humidity conditions to reduce water management system demands. However, reduced performance and enhanced degradation may occur from low electrolyte phase moisture content. In this paper, the combined current, species, and HFR distributions for a PEFC with coflow arrangement are examined under a wide range of operating inlet humidity conditions to determine the relative importance of anode and cathode humidity, provide insight into distributed performance in undersaturated inlet conditions, as well as provide supporting data for advanced model development.

Experimental

Instrumented cell design.— All experiments were performed using a segmented fuel cell with a 50 cm^2 active area. The fuel cell utilizes segmented current collector similar to that described in Mench et al.[34] Additional specific details of the fuel cell design can be found in Ref. 66. Forty-eight stainless steel landing segments for each side were embedded into electrical insulating plates made in polycarbonate plexiglass to serve as landings, and also form a flow field with single-pass serpentine overall coflow arrangement. The landings were gold-plated, and each was welded to individual silver wires to minimize contact and wire resistance. The landings of each side were divided into 12 groups, along the flow channel, with four landings in each group. Extension wires of the four landings in each group were combined together and then connected to one channel of the potentiostat. The cathode GDLs were segmented to 12 pieces along the flow channel. A resistance check, after the cell was assembled, showed that the in-plane resistances between GDL pieces were all significantly greater than 1200 mΩ. This high resistance greatly diminishes internal current spreading, and also enables distributed current and HFR measurement. For mass distribution measurements, eight species extraction ports were located at 4.3, 17.4, 30.4, 43.5, 56.5, 69.6, 82.6, and 95.7% of the fractional distance of the anode and cathode flow paths.

As shown in Fig. 1, the dimension of the flow channel is 2.16 mm wide and 3.18 mm deep, and the average pass length is approximately 71 mm. With 22 total serpentine passes formed by 48

* Electrochemical Society Student Member.
** Electrochemical Society Active Member.
z E-mail: mmm124@psu.edu

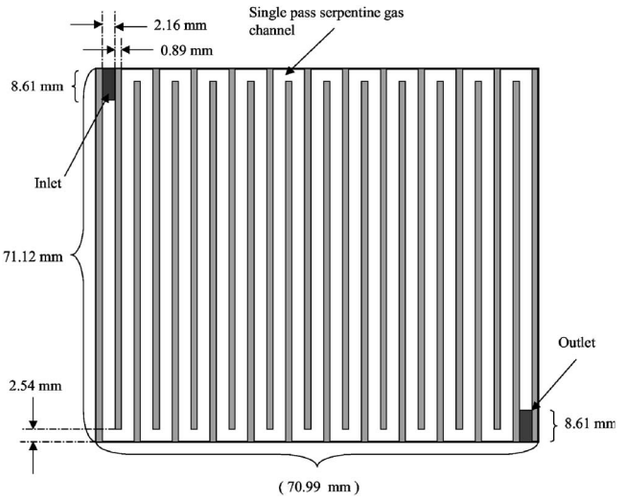

Figure 1. Schematic diagram of the instrumented fuel cell.

gold-plated landing segments, the total length of the flow channel is about 1577 mm. This single-path, deep-channel design described herein is nonoptimal from a performance standpoint, but was instead designed with computational model validation simplicity in mind.

All experiments were performed using Gore PRIMEA Series 57 membrane electrode assemblies (MEA) with a dry membrane thickness of 18 μm and a platinum loading of 0.4 mg/cm^2 on both anode and cathode. The gas diffusion medium consisted of CARBEL MP gas diffusion media as the microporous layer and Toray 060 (wetproofed) as the macroporous layer. Ultrahigh-purity (>99.999%) hydrogen and standard dry air were supplied from compressed gas cylinders.

Calculation of active area segments.— The current density data are represented at a discrete distance along the flow path, when they actually are gathered from a distributed region. To calculate the current density of an individual segment, the active area directly under the landings, and half of the adjacent gas channels, were taken. The reported discrete location of the measured current density along the flow path is the center of the total measurement area (including the area under current collection landings). This discretization gave very consistent results. Local current was measured at 12 different locations with an equivalent fractional distance from the inlet of 0.036, 0.114, 0.200, 0.286, 0.371, 0.457, 0.543, 0.629, 0.714, 0.800, 0.886, and 0.964, respectively.

Testing system.— An Arbin Systems 25-channel potentiostat/galvanostat was used to control, monitor, and measure local distributed current and high-frequency resistance (HFR) at 3 kHz. For current density measurement, the test station maintains a constant voltage while measuring the current from each segmented channel.

Table I. Baseline operating conditions.

Parameter	Value
MEA	Gore PRIMEA Series 57 MEA
Gas diffusion layer	Carbel MP gas diffusion media and Toray 060
Catalyst loading (carbon supported)	0.8 mg/cm^2 (total)
Cell temperature	80°C
Anode and cathode outlet pressure	3 atm
Cathode flow rate	1559 and 2357 sccm
Anode flow rate	367 cm^3/min
Anode gas	Ultrahigh purity H_2 (>99.999%)
Cathode gas	Commercial air (79% N_2, 21% O_2)

Table II. Relative humidity of total inlet flow.

Test Condition	Relative humidity (RH) (anode/cathode) at 80°C	Total input RH low cathode flow at 80°C	Total input RH high cathode flow at 80°C	Average current density at 0.7 V (A/cm^2)[a]
1	50/0	9.9	7.1	0.29/0.26
2	100/0	21.2	15.4	0.48/0.36
3	0/50	41.3	43.8	0.49/0.41
4	0/100	83.9	88.5	0.55/0.50
5	25/25	25.0	25.0	0.44/0.35
Baseline	100/100	100	100	0.60/0.68

[a] Lower cathode flow rate (1599 sccm)/higher cathode flow rate (2357 sccm).

The control system is equipped with dew point humidifiers, which were extensively calibrated using a desiccant and mass balance technique. To achieve different inlet relative humidities, the temperatures of the humidifiers were set by assuming 100% humidification efficiency, and the actual output water mole fraction was determined by a real-time gas analyzer (RTGA). Sources of error with this measurement can be the error in humidification used for calibration of the RTGA, imprecision in measurement of flow rate, pressure, and temperature, and some transients that can occur during apparent steady-state operation. The humidifier used for RTGA calibration was itself carefully calibrated using a dessicant absorption technique, and is described in Ref. 65. Between the humidifier and the cell, heating tapes were used to prevent condensation and maintain the desired humidification levels. Fuel cell and humidified reactant gas inlet temperatures of 80°C were maintained by model 8500 PID controllers (Omega Engineering Inc.). The cell temperature was measured by a thermocouple within the cathode backing plate.

Species measurement.— Species were measured using an Agilent Technologies RTGA as described in Ref. 65. The fuel cell was allowed to reach a steady state for each operating condition prior to species data collection. All species collection data were taken at a cell potential of 0.7 V. The sample line to the RTGA was maintained well above 100°C to prevent condensation and loss of proper mole fraction precision. In a few cases, an Agilent 3000 Micro GC was used to record test data, as described in Ref. 64.

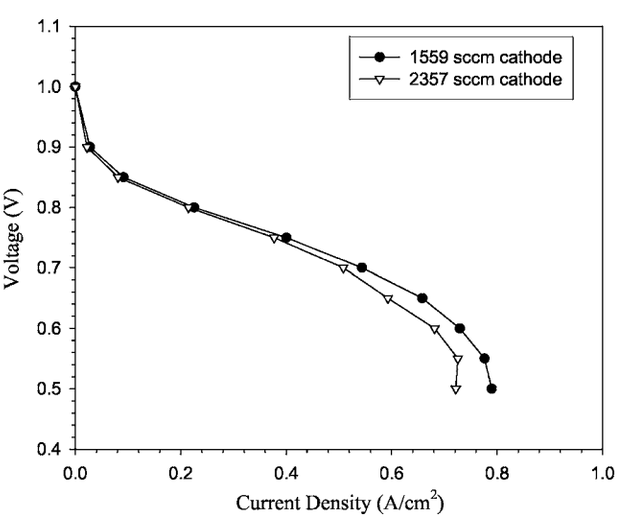

Figure 2. Steady-state polarization curve for condition 3. RH = 0/100 anode/cathode.

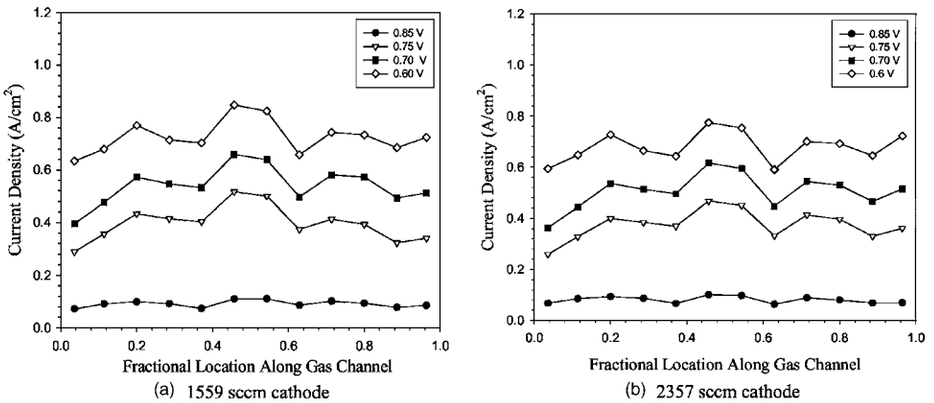

Figure 3. Distributed steady-state current density as a function of cell location for condition 4. RH = 0/100 anode/cathode.

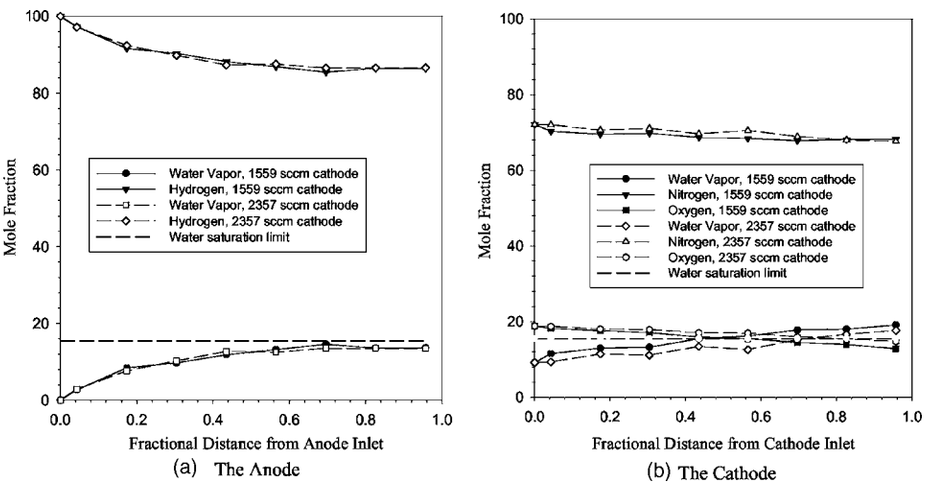

Figure 4. Distributed steady-state species distribution on the anode and cathode for condition 4. RH = 0/100 anode/cathode. Data taken at steady state, 0.7 V.

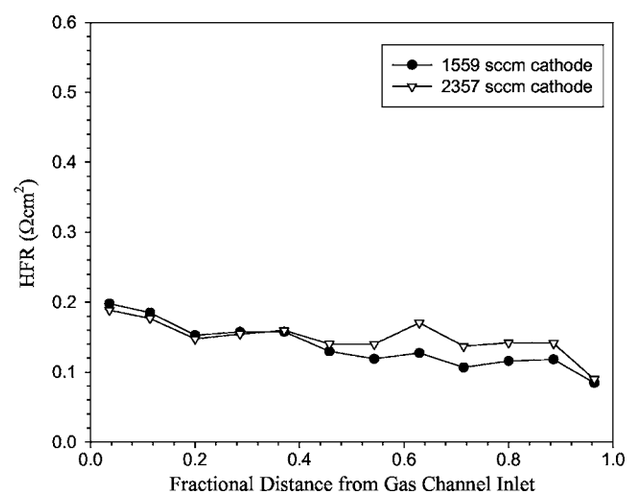

Figure 5. Distributed steady-state high-frequency resistance distribution for condition 4. RH = 0/100 anode/cathode, 0.7 V. Data taken at steady state, 0.7 V.

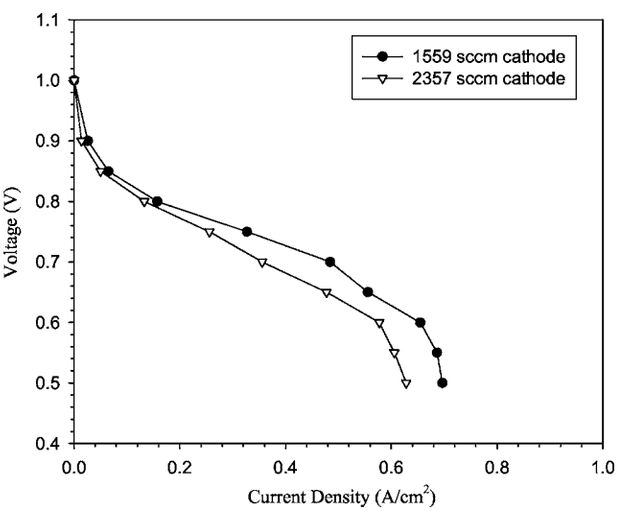

Figure 6. Bulk polarization curves for condition 2. RH = 100/0 anode/cathode.

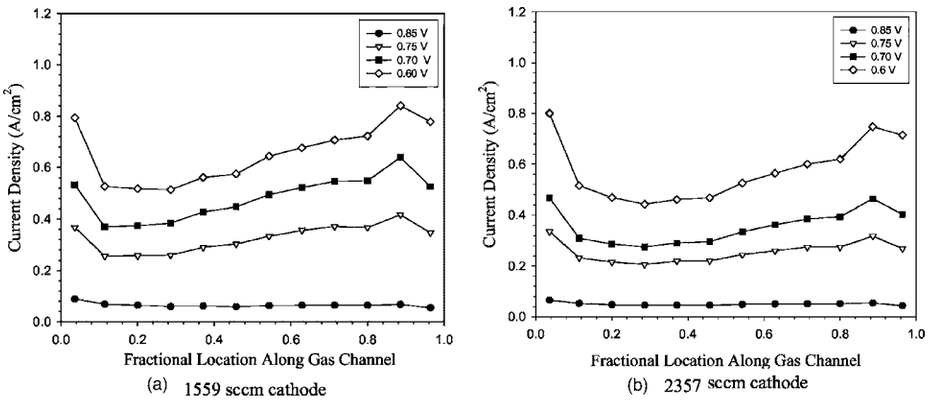

Figure 7. Distributed steady-state current density as a function of cell location for condition 2. RH = 100/0 anode/cathode.

Operating conditions.— Tests were conducted at baseline operating conditions given in Table I, with varying inlet flow rates and relative humidities. Table II shows the five different conditions chosen for study of anode and cathode inlet relative humidity effects. The bulk performance of a fully humidified condition is also listed as a benchmark reference. Tests were conducted with a constant flow rate on the anode and cathode. Constant reactant flow rate was chosen because it is more convenient for model validation and interpretation of results. Experiments were performed at two different dry air flow rates on the cathode of 1599 and 2357 sccm (standard referenced at 0°C). For comparison, these constant flow rates represent a stoichiometry of 2.4 and 3.6, respectively, at a current density of 0.8 A/cm^2. The dry hydrogen flow rate on the anode was kept constant in all experiments at 367 sccm, which represents a stoichiometry of 1.3 at 0.8 A/cm^2. Pressure drops through the fuel cell were measured for different gas flow rates under fully humidified conditions. Small pressure drops, 0.34 psi (0.023 atm or 2.3 kPa) for the 2357 sccm cathode flow rate and 0.023 psi (0.0016 atm or 0.16 kPa) for the 367 sccm anode flow rate, indicate that the pressure change along the flow path had a negligible effect on water content for the flow-field design and operation conditions tested.

At each operating condition, current density, species, and HFR profiling was measured after steady state was achieved (>30 min for most cases). After reaching steady state, current measurements were taken once per second for 5 min, and an average local current density was calculated from the 300 data points taken for each location, at each voltage. For all test conditions, a distributed high-frequency (3 kHz) resistance measurement was taken at 0.7 V. Additional HFR data were obtained for comparison at 10 kHz using a Solatron 1255b frequency response analyzer on three segments (inlet, center, and outlet of fuel cell). The 10 kHz resistance measured was nearly identical to the value obtained at 3 kHz for the conditions tested. Therefore, 3 kHz was deemed to be sufficiently high.

Results and Discussion

Bulk performance.— In order to analyze the results, it is useful to normalize the test conditions to the total relative humidity of the bulk flow. This way, the total water input to the fuel cell for the various conditions can be compared without ambiguity. Table II shows the overall relative humidity input, derived by combining anode and cathode inlet flows at both the high and low cathode flow rate conditions. For example, condition 1, anode/cathode relative humidity (A/C RH = 50/0) has about one-sixth to one-fourth the total relative humidity value of condition 3 (A/C RH = 0/50) in the cell, despite the same individual reactant relative humidity percentages. This is a result of the higher cathode flow rate compared to the anode. It is clear that for undiluted hydrogen and air flow, an identical anode and cathode relative humidity will have a far greater molar rate of water entering from the cathode than the anode. Therefore, condition 5 (A/C RH = 25/25) is a relatively dry cathode inlet condition, even though the values of the relative humidity on both inlets are the same.

Low anode humidity operation.— According to the test matrix in Table II, four series of tests were conducted with inlet anode humidity less than 100%. Test condition 4 is most illustrative of an undersaturated inlet anode effect because, for this test series, the cathode inlet was fully humidified, while the anode was fully dry. Figures 2 and 3 show the bulk polarization and distributed current density plots as a function of location for this test condition, respectively. Due to small variations of local compression, there is some

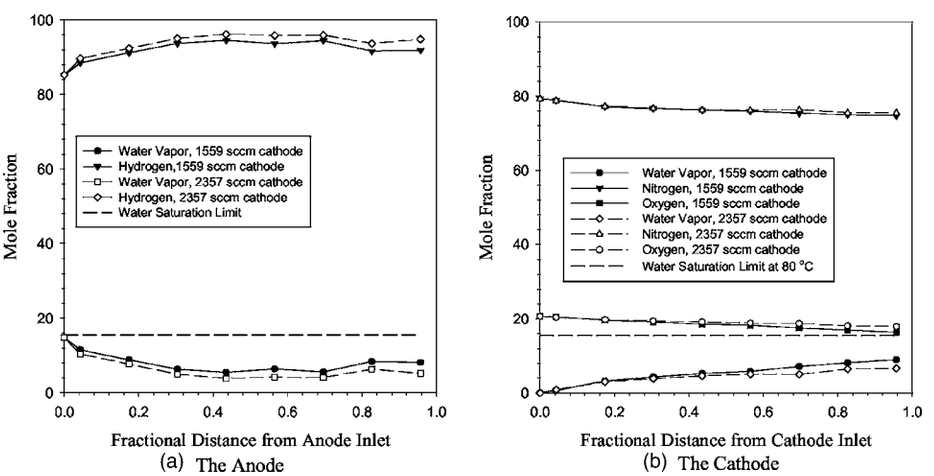

Figure 8. Distributed steady-state species distribution on the anode and the cathode for condition 2. RH = 100/0 anode/cathode. Data taken at steady state, 0.7 V.

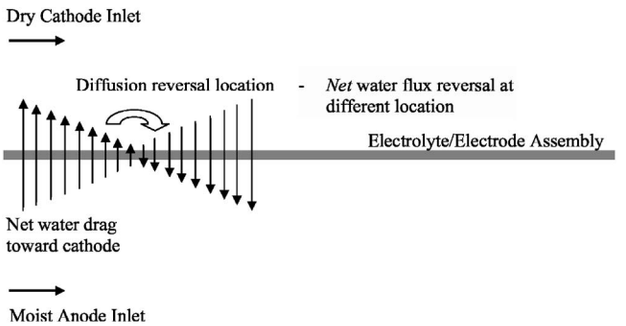

Figure 9. Illustration of the diffusion reversal process in the electrolyte occurring for undersaturated inlet cathode conditions, resulting in locally varying current phenomenon.

scatter in the measured local current density, an overall increasing to a maximum, then a decreasing trend can be seen in Fig. 3. The bulk (Fig. 2) and local (Fig. 3) performance of the high- and low cathode flow rate conditions are very similar until high current density, when the low flow rate cathode condition has slightly increased local performance, despite less input water molar rate.

Figure 4 are the distributed steady-state species distributions at 0.7 V for condition 4 for the anode and cathode. On the anode side, the anode water content increases almost monotonically to saturation due to uptake, and the hydrogen mole fraction concomitantly decreases along the flow path, as the only other major species in the anode. In the cathode, both the nitrogen and the oxygen content decrease as the water vapor mole fraction increases. At the inlet the current density is low, depressing drag and generation, while the concentration gradient for diffusion is at a maximum at this location. Toward the exit of the serpentine channel in both flow rate cases, the cathode flow apparently saturates, reaching a plateau around 16% mole fraction, slightly higher than the saturated water mole fraction at this test conditions. As described previously, although the backing plate temperature was controlled to 80°C by the thermocouple, gas temperature in the flow path can be higher due to waste heat generation. Therefore, the exit gas can appear oversaturated compared to the setpoint temperature of 80°C.

Figure 5 shows the distributed steady-state HFR for test condition 4 at 0.7 V. Reversing the general trend of the anode-side water vapor content, there is an overall decreasing trend in the cell resistance with location along the flow path, corresponding to increased electrolyte water content in the electrolyte and catalyst layers as the anode-side water mole fraction increases. There is nearly a 100% decrease in resistance of the cell from inlet to outlet. The data show that the HFR for the low-flow condition is higher at the inlet of the cell due to the lower combined RH at the inlet (84 to 88%, respectively). However, the reaction-generated water humidifies the low-flow gas streams more due to the lower cathode flow rate, which

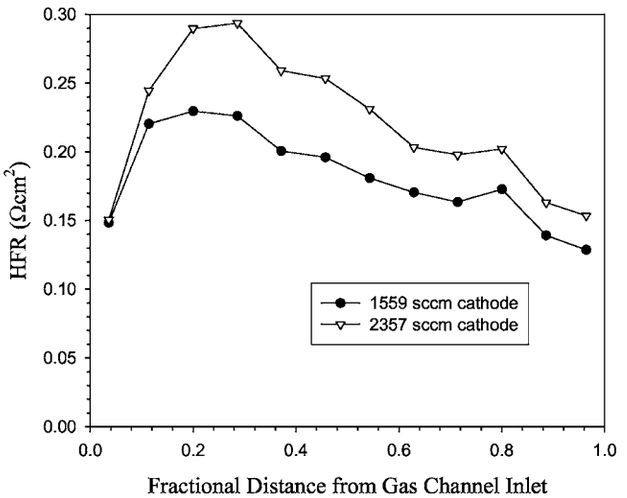

Figure 10. Distributed steady-state high-frequency resistance distribution for condition 2. RH = 100/0 anode/cathode. Data taken at steady state, 0.7 V.

results in a higher hydration of the membrane and a lower HFR. This observation is in agreement with the total cell performance shown in Fig. 2 and 3.

The distributed current, water vapor, and HFR data for the other low anode humidity condition 3 follows a similar overall increasing (current, water vapor) and decreasing (HFR) trend, indicating that the distributed performance is strongly related to the anode-side water vapor content.

Low cathode humidity operation.— According to the test matrix in Table II, four series of tests were conducted with reduced cathode humidity. Test condition 2 is most representative of an undersaturated inlet cathode effect because, for this test series, the anode inlet was fully humidified and the cathode inlet dry. Figure 6 and Fig. 7 show the bulk polarization and distributed current density plots as a function of location for this test condition, respectively. In this case the higher dry cathode flow rate has much lower bulk performance, due to increased drying from the zero inlet humidity cathode flow. Compared to the fully humidified cathode condition of condition 4 (A/C RH = 0/100), condition 2 (A/C RH = 100/0) has a much lower combined inlet relative humidity; therefore, condition 2 is much dryer overall compared to condition 4. Note the local current density profile is very different for a dry anode condition than for the dry cathode condition 2. Instead of an overall local performance increse, local current density is initially high, dips to a minimum, and then gradually increases up to a maximum. This resulting decrease to a local minimum, then increasing trend, is observed for all cases with a dry or low relative humidity cathode compared to that

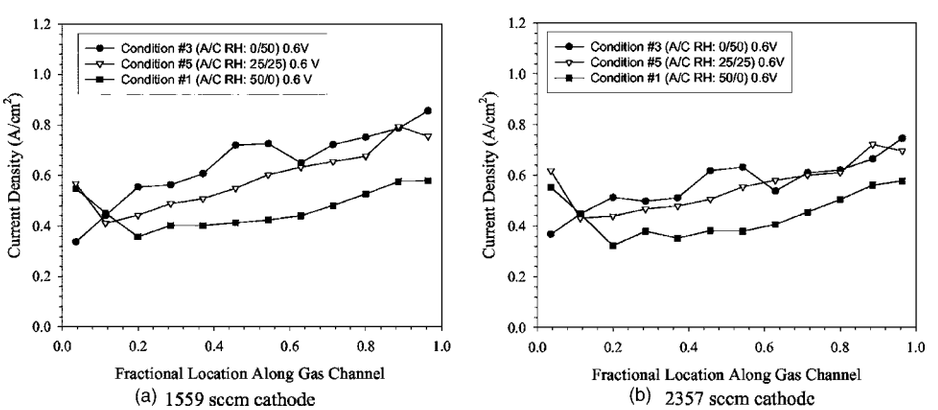

Figure 11. Comparison of current density distributions for several different conditions at two cathode flow rates.

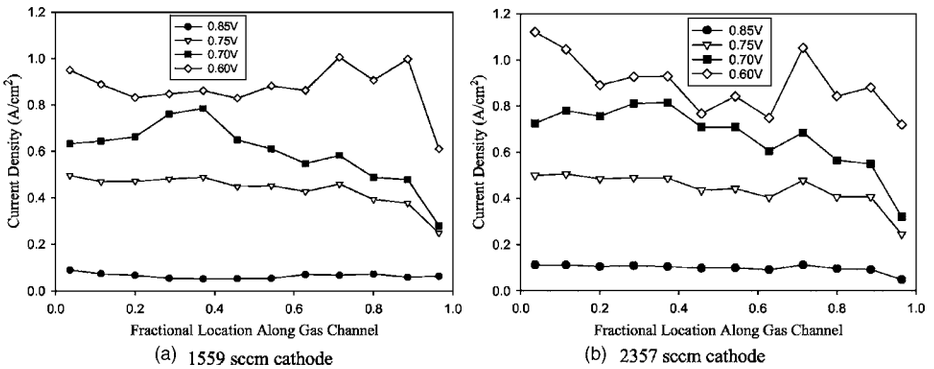

Figure 12. Distributed steady-state current density as a function of cell location for fully humidified condition. RH = 100/100 anode/cathode.

of the anode. This is in agreement with modeling results from Van Zee et al.[67] and Wang et al.[68] The general trend found was that more water overall input to the cell resulted in greater bulk performance. However, it is clear that local anode dryout can occur, and anode humidification is necessary, to avoid local dryout and poor performance that can also lead to accelerated degradation near the anode inlet location.

Figure 8 shows the distributed steady state-species distributions for condition 2 for the anode and cathode. In the cathode, both the nitrogen and the oxygen content decrease, as the water vapor mole fraction increases. The anode-side distribution is most interesting. At the inlet of the anode for a dry cathode case, there is a dip in the vapor fraction along the gas channel until a minima is reached, then the vapor fraction increases, creating a very similar decrease to a local minima, then increasing trend compared to the local current distribution trend of Fig. 7.

The decreasing-increasing profile phenomenon is mainly a result of a diffusion reversal process between the anode and cathode for underhumidified cathode conditions, as schematically shown in Fig. 9. Near the inlet, where the cathode is underhumidified compared to the anode, all modes of water transport are toward the cathode (electro-osmotic drag and diffusion), and generation is of course at the cathode. At locations further along the single serpentine path, the water activity at the cathode increases above that of the anode, and the direction of diffusion mass transport reverses, eventually overcoming electro-osmotic drag and initiating a net flux of water back toward the anode. This water mass flux reversal results in the rehumidification of the anode flow path observed. Additionally, the higher oxygen fractional pressure at the inlet for dry cathode conditions also increases the local current density to some extent. Note that the diffusion flux reversal location and location of net water mass flux reversal is not the same, as the net water flux reversal point is also a function of the electro-osmotic drag (and therefore current).

Figure 10 shows the distributed steady-state HFRs for test condition 2 at 0.7 V. In this case, the anode-side water content has a strong effect on the HFR profile. The HFR trend roughly inverses the decreasing-increasing profile observed for anode water vapor content. At the beginning, following the decreasing trend of the anode-side water vapor content, there is an increasing trend in the cell resistance with location along the flow path, although the cathode-side channel-level water vapor content increases. Further downstream, the HFR decreases as the anode water content increases. However, it should be noticed that the local resistance maxima are earlier than the local anode water content minima due to the increasing cathode water content. In fact, it is evident that before diffusion reversal, there is localized anode dryout caused by diffusion and migration of water from the anode. The dryout, evident even for the ultrathin 18 μm electrolytes used, results in increased impedance that drives down local current density. The humidification condition of a dry cathode is commonly much better than a dry anode, even with a dry inlet condition, due to water generation at the cathode catalyst layer. Anode moisture profile has a more pronounced effect on the local current profile (through the local HFR) than the cathode vapor profile.

For the higher cathode flow rate, the increase in local HFR is greater than the low cathode flow rate case. This corresponds to the decreased anode water vapor content caused by increased diffusion to the dry cathode for higher flow rate. Note that the inlet region HFR for condition 2 (Fig. 10) is 25% lower than the initial HFR for condition 4 (Fig. 5), despite much higher inlet bulk relative humidity for condition 4. This indicates the importance of maintaining high inlet anode humidity for increased inlet performance, and avoidance of local anode inlet dryout that has been implicated in pinhole formation and concomitant performance degradation.

Other low-humidity test condition comparisons.— For all other test cases, the results follow the same characteristic trends described for low anode or cathode humidity operation. All other test cases fall between the extremes of conditions 2 and 4. Figure 11 shows comparisons of the current profiles for other conditions 1, 3, and 5, respectively. Condition 1 (A/C RH 50/0) and condition 5 (A/C RH = 25/25) are relatively dry cathode inlet conditions. Condition 3 (A/C RH 0/50) is a relatively dry anode inlet condition. The decreasing-increasing profile is evident for the two dry cathode cases, and a generally increasing trend in local current is shown for the dry anode case (condition 3).

Note, from Fig. 11, that condition 3 (A/C RH = 0/50) is the test condition with the greatest total water content at the inlet for these three cases, but it is all at the cathode. This is also the condition with the worst local performance at the inlet region, although its average

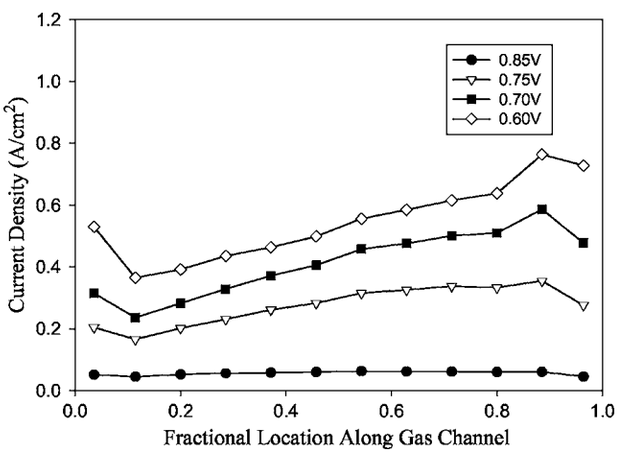

Figure 13. Distributed steady-state current density as a function of cell location for a constant stoichiometry operation. Condition 5, RH = 25/25 anode/cathode, anode stoichiometry = 1.2, and cathode stoichiometry = 2.0.

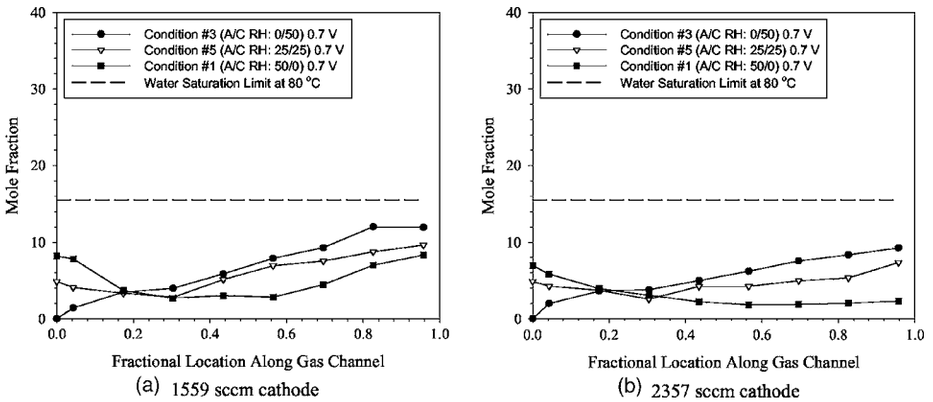

Figure 14. Comparison of anode water vapor profile for several different conditions at two cathode flow rates. Data taken at steady state, 0.7 V.

bulk performance is the best among the three cases. In contrast, condition 2 (A/C RH = 500) has the least total water content at the inlet and has the best local performance in this region. However, it suffers the lowest overall bulk averaged performance. Although in these cases the greater amount of water resulted in better bulk performance, even better performance and avoidance of anode dryout can be achieved with some moisture at the anode inlet.

Even for a test case of complete inlet saturation (A/C RH = 100/100), the authors have observed a similar anode dryout at high current densities (>1.0 A/cm^2), as shown in Fig. 12. Since it is possible that electrolyte dryout exacerbates the physical degradation of the electrolyte, the need for high anode humidification at the inlet of the flow field (although bulk performance may improve only slightly) is clear. It is anticipated that the trends observed for this single path serpentine flow field would be maintained for parallelized concurrent flow as well, and ongoing study is verifying this. Additionally, although these trends are shown for constant flow rate, the authors have verified substantively identical qualitative trends for constant stoichiometry conditions. Figure 13 shows a current distribution result for condition 5 with constant stoichiometry rather than constant flow rate, and in all such cases a similar qualitative trend was observed comparing relatively dry anode and cathode cases to the constant flow rate cases.

The species distribution comparisons at 0.7 V for two cathode flow rates for the three cases 1,3, and 5 are shown in Figs. 14 and 15 and follow the trends noted before to different degrees, depending on the water imbalance. Anode channel-level water vapor profile is the rough qualitative inverse of the current profile, while the cathode profile is not, again indicating that the anode moisture profile strongly influences the local current distribution.

The HFR data shown in Fig. 16 are also consistent, and confirm the performance variation is strongly linked to anode gas-channel moisture profile. Note the differences between the two flow rates of the HFR plots. For the dry cathode case, a higher dry cathode flow rate results in an increased HFR, while for the dry anode case, higher cathode flow rate decreases the bulk HFR. Simply stated, the more water, the lower the overall HFR, although the inlet region is most influenced by the anode condition, and distributed profiles vary greatly.

Generalized distributed performance.— Based on the data generated, a generalized performance plot for undersaturated inlet current distribution with a concurrent flow field can be constructed. Performance is highly coupled to the anode-side water vapor content in the inlet region through the local electrolyte conductivity, indicating electro-osmotic drag acts to dry the anode side and is not completely compensated for by back-diffusion, even for the thin 18 μm electrolytes used. This demonstrates that the anode water profile contributes significantly to the overall performance of a fuel cell inlet with undersaturated inlet flow.

Figure 17 is a sketch of the generic relative current versus location along the flow channel for different combinations of inlet humidity on the anode and cathode, and is key to understanding local performance. The generalized performance curve is qualitatively sinusoidal in shape (although not necessarily symmetric or with equal amplitude or wavelength, as shown for convenience).

Region I begins at the inlet of the fuel cell. If the anode is dryer than the cathode and the current is relatively low, the net flux of water is always neutral or toward the anode, resulting in an increasing performance through region I. The steepness of the slope of this portion is exacerbated with increased moisture imbalance between anode and cathode, increased current density, and other thermodynamic and geometric parameters. In contrast, if the water vapor imbalance initially favors the anode (dryer cathode), diffusion and electro-osmotic drag are both initially toward the cathode, resulting in a drying condition at the anode catalyst layer and electrolyte,

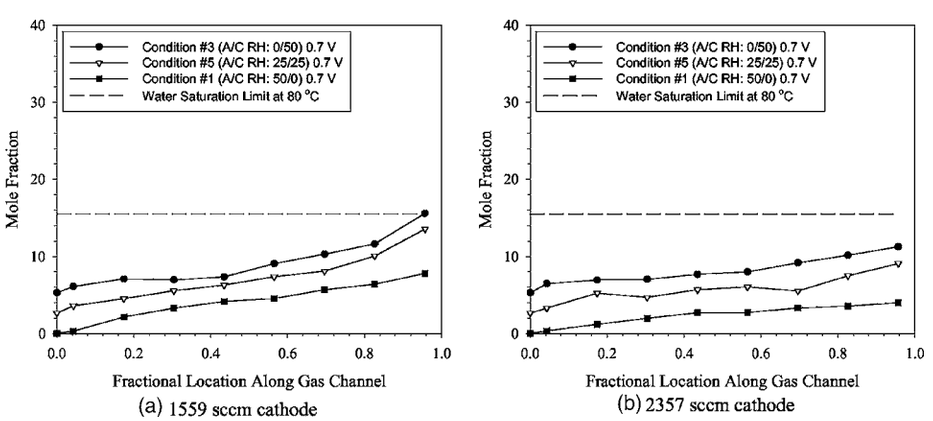

Figure 15. Comparison of cathode water vapor profile for several different conditions at two cathode flow rates. Data taken at steady state, 0.7 V.

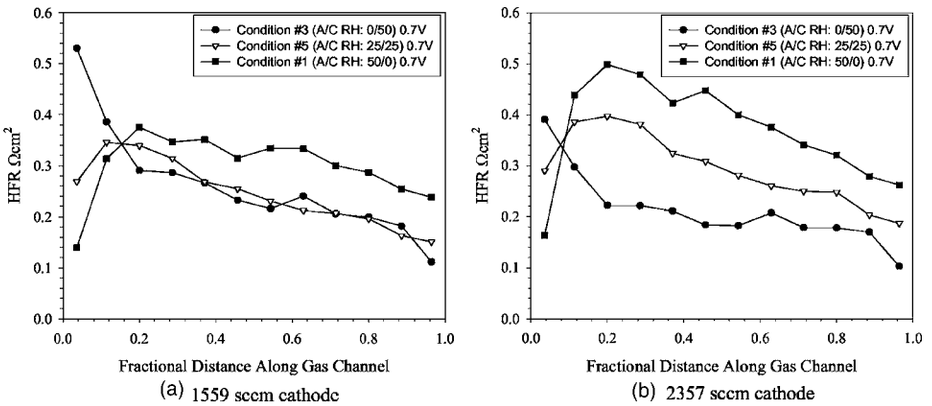

Figure 16. Comparison of high-frequency resistance profile at 3 khz for several different conditions at two cathode flow rates. Data taken at steady state, 0.7 V.

reducing performance until a local minima is reached, which terminates region I. The minimum in performance is exacerbated by increased current density and moisture difference between anode and cathode, as well as flow rates and other thermodynamic and geometric parameters. Note that, for closely hydrated anode and cathode at low to moderate current density, performance in region I can be homogeneous, as illustrated in Fig. 17. Note that the end of region I is shown as the same location for dry anode and dry cathode conditions, when this is not necessarily the case. In fact, region II for a relatively dry anode inlet is really a continuation of region I and no discrete boundary between the two regions is defined.

In region II, the case with relative dry anode feeding continues increasing performance to a maximum (if reached), that ends region II. The decrease from the maximum current is a result of decreasing reactant availability or flooding, and depends on operating conditions, and therefore may not be severe as shown in Fig. 17. The dry relative cathode case begins region II at the point of water mass flux reversal from cathode to anode results. In this situation, this reversal may not occur with a thick electrolyte if back-diffusion never overcomes electro-osmotic drag to the cathode. This flux reversal reduces anode-side dryout performance loss and initiates an increase in performance. Due to time-varying upstream temperature effects, the precise location of the mass flux reversal may fluctuate, causing bulk performance instability. This effect was observed over extended periods in testing with low inlet cathode humidity, and is the subject of continued investigation and analysis. For both the dry relative anode and cathode cases, region II concludes with a maximum in performance, if reached at all. Note that the location of the maxima is dependent on the fuel cell and operating conditions, as discussed, and is therefore not the same for the different humidity cases, as shown in Fig. 17 for simplicity.

In region III, for convenience, both dry anode and cathode cases are shown to peak at the same location, although this depends on the individual conditions and is not necessarily the case. Following the maximum local current, there is a downward trend resulting from local flooding or gas-phase mass transport losses at the electrode(s). This peak and downward trend will only occur if a reactant starvation condition (via flooding or high utilization) is reached.

The generalized performance curve of Fig. 17 closely follows anode gas-channel water vapor content through region II, indicating anode catalyst layer and electrolyte moisture content plays a key role in controlling the distributed performance of an undersaturated inlet PEFC. Cathode conditions are generally locally moist at the catalyst layer, and control the location of the maximum performance which initiates region III. The region I trend depends on the side with greatest hydration and local water activity. The amplitude of the peaks is increased with increasing current density and water imbalance between anode and cathode at the inlet. The width of regions I-III depends on current density, flow rate, water imbalance, and membrane and electrode thickness as well. As discussed, the same general trends in local performance for various humidity combinations is achieved for constant stoichiometry conditions, but is too much coverage for a single publication. It is quite difficult to achieve homogeneous performance at high current density (>0.5 A/cm^2) with basic humidification schemes and cocurrent flow. Either the inlet is dry and performance is depressed, or the outlet is flooded, or both.

Conclusions

Experimental data including species, current, and impedance distributions in a PEFC with single-path coflow configuration have been obtained over a wide range of operating humidity and flow rates. Results indicate that anode humidity has strong effect on the current distribution (CD) in the inlet region, through the ionic resistance, under low-humidity conditions. The CD curves are qualitatively similar to H_2O mole fraction distribution in the anode, and the HFR profile data confirm that the CD is strongly affected by the anode side dryout, even for the thin 18 μm electrolytes used. For a coflow low-humidity cathode condition, local performance and anode water vapor content follow a decrease to a local minimum, and then an increasing trend resulting from a net water flux reversal from the anode to the cathode.

For the low-humidity conditions tested, the bulk performance was generally higher with increased total inlet moisture content. However, humidification of the anode, rather than the cathode, was demonstrated to be most critical to achieve high inlet region performance, even with more than twice the water content available at the cathode inlet. This has important implications in limiting performance degradation, where local anode dry out may be linked to the formation of pinholes in the electrolyte near the anode inlet.

A generalized local current distribution was constructed to show the expected qualitative shape of the coflow current profile for a wide range of inlet humidity conditions, with amplitude of local

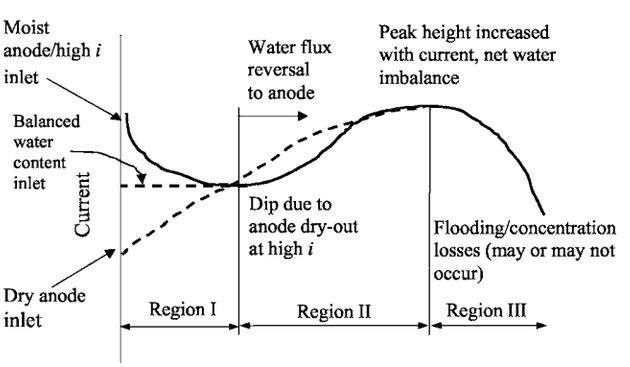

Figure 17. Characteristic local current curve for undersaturated inlet conditions.

peaks and valleys dependent on current, flow rate, initial water imbalance between anode and cathode, and other thermodynamic and geometric parameters. These data demonstrate the importance of the anode water vapor distribution and back-diffusion, and can be used to guide water management systems for more efficient water injection, and also should be highly useful for detailed validation of computational modeling.

Acknowledgments

The financial support of W.L. Gore and Associates, Incorporated, is gratefully acknowledged. The RTGA used in this study was supplied under a grant from Agilent Technologies, Incorporated.

Pennsylvania State University assisted in meeting the publication costs of this article.

References

1. D. M. Bernardi, *J. Electrochem. Soc.*, **137**, 3344 (1990).
2. A. Parthasarathy, S. Srinivasan, A. J. Appleby, and C. Martin, *J. Electrochem. Soc.*, **139**, 2856 (1992).
3. A. Parthasarathy, S. Srinivasan, A. J. Appleby, and C. Martin, *J. Electrochem. Soc.*, **139**, 2530 (1992).
4. Y. W. Rho, O. A. Velev, S. Srinivasan, and Y. T. Kho, *J. Electrochem. Soc.*, **141**, 3838 (1994).
5. J. C. Amphlett, R. M. Baumert, R. F. Mann, B. A. Peppley, P. R. Roberge, and T. J. Harris, *J. Electrochem. Soc.*, **142**, 9 (1995).
6. R. Mosdale and S. Srinivasan, *Electrochim. Acta*, **40**, 413 (1995).
7. H.-F. Oetjen, V. M. Schmidt, U. Stimming, and F. Trila, *J. Electrochem. Soc.*, **143**, 3838 (1996).
8. F. N. Büchi and D. Srinivasan, *J. Electrochem. Soc.*, **144**, 2767 (1997).
9. F. A. Uribe, S. Gottesfeld, and T. A. Zawodzinski, *J. Electrochem. Soc.*, **149**, A293 (2002).
10. E. A. Ticianelli, C. R. Derouin, and S. Srinivasan, *J. Electroanal. Chem. Interfacial Electrochem.*, **251**, 275 (1988).
11. T. E. Springer, T. A. Zawodzinski, M. S. Wilson, and S. Gottesfeld, *J. Electrochem. Soc.*, **143**, 587 (1996).
12. E. Antolini, R. R. Passos, and E. A. Ticianelli, *J. Appl. Electrochem.*, **32**, 383 (2002).
13. M. Fournier, J. Hamelin, K. Agbossou, and T. K. Bose, *Fuel Cells*, **2**, 117 (2002).
14. L. Wang, A. Husar, T. Zhou, and H. Liu, *Int. J. Hydrogen Energy*, **28**, 1263 (2003).
15. J. Larminie and A. Dicks, *Fuel Cell Systems Explained*, John Wiley & Sons, ltd., New York (2002).
16. S. Gottesfeld, in *Advances in Electrochemical Science and Engineering*, C. Tobias, Editor, Vol. 5, Wiley & Sons, New York (1997).
17. T. E. Springer, T. A. Zawodinski, and S. Gottesfeld, *J. Electrochem. Soc.*, **138**, 2334 (1991).
18. D. M. Bernardi and M. W. Verbrugge, *AIChE J.*, **37**, 1151 (1991).
19. D. M. Bernardi and M. W. Verbrugge, *J. Electrochem. Soc.*, **139**, 2477 (1992).
20. T. E. Springer, M. S. Wilson, and S. Gottesfeld, *J. Electrochem. Soc.*, **140**, 3513 (1993).
21. T. F. Fuller and J. Newman, *J. Electrochem. Soc.*, **140**, 1218 (1993).
22. T. V. Nguyen and R. E. White, *J. Electrochem. Soc.*, **140**, 2178 (1993).
23. C. Y. Wang and W. B. Gu, *J. Electrochem. Soc.*, **145**, 3407 (1998).
24. V. Gurau, H. Liu, and S. Kakac, *AIChE J.*, **44**, 2410 (1998).
25. J. S. Yi and T. V. Nguyen, *J. Electrochem. Soc.*, **146**, 38 (1999).
26. S. Um, C. Y. Wang, and K. S. Chen, *J. Electrochem. Soc.*, **147**, 4485 (2000).
27. Z. H. Wang, C. Y. Wang, and K. S. Chen, *J. Power Sources*, **94**, 40 (2001).
28. Q. Guo, V. A. Sethuraman, and R. E. White, *J. Electrochem. Soc.*, **151**, A983 (2004).
29. A. A. Kulikovsky, J. Divisek, and A. A. Kornyshev, *J. Electrochem. Soc.*, **146**, 3981 (1999).
30. S. Um and C. Y. Wang, *J. Power Sources*, **125**, 40 (2004).
31. P. Berg, K. Promislow, J. Pierre, J. Stumper, and B. Wetton, *J. Electrochem. Soc.*, **151**, A341 (2004).
32. L. Pisani, G. Murgia, M. Valentini, and B. D' Aguanno, *J. Electrochem. Soc.*, **149**, A898 (2002).
33. A. Z. Weber and J. Newman, *J. Electrochem. Soc.*, **151**, A311 (2004).
34. M. M. Mench, C. Y. Wang, and M. Ishikawa, *J. Electrochem. Soc.*, **150**, A1052 (2003).
35. M. Noponen, J. Ihonen, A. Lundblad, and G. Lindbergh, *J. Appl. Electrochem.*, **34**, 255 (2004).
36. M. M. Mench and C. Y. Wang, *J. Electrochem. Soc.*, **150**, A79 (2003).
37. M. Noponen, T. Mennola, M. Mikkola, T. Hottinen, and P. Lund, *J. Power Sources*, **106**, 304 (2002).
38. D. J. L. Brett, S. Atkins, N. P. Brandon, V. Vesovic, N. Vasileiadis, and A. R. Kucernak, *Electrochem. Commun.*, **3**, 628 (2001).
39. C. Wieser, A. Helmbold, and E. Gülzow, *J. Appl. Electrochem.*, **30**, 803 (2000).
40. A. B. Geiger, R. Eckl, A. Wokaun, and G. G. Scherera, *J. Electrochem. Soc.*, **151**, A394 (2004).
41. J. Stumper, S. Campell, D. Wilkinson, M. Johnson, and M. Davis, *Electrochim. Acta*, **43**, 3773 (1998).
42. S. Cleghorn, C. Derouin, M. Wilson, and S. Gottesfeld, *J. Appl. Electrochem.*, **28**, 663 (1998).
43. D. M. Bernardi, *J. Electrochem. Soc.*, **137**, 3344 (1990).
44. T. E. Springer, T. A. Zawodzinski, and S. Gottesfeld, *J. Electrochem. Soc.*, **138**, 2334 (1991).
45. D. M. Bernardi and M. W. Verbrugge, *J. Electrochem. Soc.*, **139**, 2477 (1992).
46. T. F. Fuller and J. Newman, *J. Electrochem. Soc.*, **140**, 1218 (1993).
47. M. Eikerling, Y. I. Kharkats, A. A. Kornyshev, and Y. M. Volfkovich, *J. Electrochem. Soc.*, **145**, 2684 (1999).
48. J. S. Yi and T. V. Nguyen, *J. Electrochem. Soc.*, **146**, 38 (1999).
49. I.-M. Hsing and P. Futerko, *Chem. Eng. Sci.*, **55**, 4209 (2000).
50. J. J. Baschuk and X. Li, *J. Power Sources*, **86**, 181 (2000).
51. Z. H. Wang, C. Y. Wang, and K. S. Chen, *J. Power Sources*, **94**, 40 (2001).
52. D. Natarajan and T. V. Nguyen, *J. Electrochem. Soc.*, **148**, A1324 (2001).
53. L. You and H. Liu, *Int. J. Heat Mass Transfer*, **45**, 2277 (2002).
54. C. Y. Wang, in *Handbook of Fuel Cells-Fundamentals, Technology and Applications*, W. Lietsich, A. Lamm, and H. A. Gasteiger, Editors, Vol. 3, Part 3, p. 337, John Wiley & Sons, Chichester (2003).
55. K. Tuber, D. Pocza, and C. Hebling, *J. Power Sources*, **124**, 403 (2003).
56. J. H. Nam and M. Kaviany, *Int. J. Heat Mass Transfer*, **46**, 4595 (2003).
57. D. Natarajan and T. V. Nguyen, *J. Power Sources*, **115**, 66 (2003).
58. T. V. Nguyen and M. W. Knobbe, *J. Power Sources*, **114**, 70 (2003).
59. U. Pasaogullari and C. Y. Wang, *J. Electrochem. Soc.*, **151**, A399 (2004).
60. W.-k. Lee, J. W. Van Zee, S. Shimpalee, and S. Dutta, in *Proceedings of ASME Heat Transfer Division*, 1, 339 (1999).
61. G. J. Janssen, *J. Electrochem. Soc.*, **148**, A1313 (2001).
62. G. J. Janssen and M. L. Overvelde, *J. Power Sources*, **101**, 117 (2001).
63. X. Ren and S. Gottesfeld, *J. Electrochem. Soc.*, **148**, A87 (2001).
64. M. M. Mench, Q. L. Dong, and C. Y. Wang, *J. Power Sources*, **124**, 90 (2003).
65. Q. Dong, J. Kull, and M. M. Mench, *J. Power Sources*, **139**, 106 (2005).
66. O. H. Finckh, M.S. Thesis, The Pennsylvania State University University Park, PA (2002).
67. W.-k. Lee, S. Shimpalee, and J. W. Van Zee, *J. Electrochem. Soc.*, **150**, A341 (2003).
68. H. Ju, C. Y. Wang, S. Cleghorn, and U. Beuscher, *J. Electrochem. Soc.*, **152**, A1645 (2005).